Physics of Arctic landfast sea ice and implications on the cryosphere: an overview

ZHAI Mengxi[1*], Matti LEPPÄRANTA[2], Bin CHENG[3], LEI Ruibo[1] & ZHANG Fanyi[1]

[1] Key Laboratory of Polar Science, MNR, Polar Research Institute of China, Shanghai 200136, China;
[2] University of Helsinki, Helsinki Fi-00014, Finland;
[3] Finnish Meteorological Institute, Helsinki Fi-00101, Finland

Abstract Landfast sea ice (LFSI) is a critical component of the Arctic sea ice cover, and is changing as a result of Arctic amplification of climate change. Located in coastal areas, LFSI is of great significance to the physical and ecological systems of the Arctic shelf and in local indigenous communities. We present an overview of the physics of Arctic LFSI and the associated implications on the cryosphere. LFSI is kept in place by four fasten mechanisms. The evolution of LFSI is mostly determined by thermodynamic processes, and can therefore be used as an indicator of local climate change. We also present the dynamic processes that are active prior to the formation of LFSI, and those that are involved in LFSI freeze-up and breakup. Season length, thickness and extent of Arctic LFSI are decreasing and showing different trends in different seas, and therefore, causing environmental and climatic impacts. An improved coordination of Arctic LFSI observation is needed with a unified and systematic observation network supported by cooperation between scientists and indigenous communities, as well as a better application of remote sensing data to acquire detailed LFSI cryosphere physical parameters, hence revolving both its annual cycle and long-term changes. Integrated investigations combining *in situ* measurements, satellite remote sensing and numerical modeling are needed to improve our understanding of the physical mechanisms of LFSI seasonal changes and their impacts on the environment and climate.

Keywords landfast sea ice, **Arctic Ocean**, **remote sensing**, **mass balance**

1 Introduction

Climate change severely impacted the Arctic Ocean and is amplified over the Arctic; Arctic surface temperature has increased over twice the global average (Meredith et al., 2019). Arctic sea ice extent has been decreasing dramatically in summer (Peng et al., 2018), and is becoming thinner and younger (Kwok, 2018; Onarheim et al., 2018).

Landfast sea ice (LFSI) is the sea ice that forms and remains fast along the coast, where it is attached to the shore, to an ice wall, to an ice front, between shoals or grounded icebergs. (WMO, 2014). Unlike drift ice, LFSI does not move with currents and winds. Though accurate in definition, it does not explicitly state the length of time for which ice must remain stationary before it is classed as 'fast'. This is because, in many regions, LFSI breaks off from the shore and reforms several times each season (Massom et al., 2009). For the Arctic, Mahoney et al. (2005) defined LFSI as sea ice that is contiguous with the land and

* Corresponding author, ORCID: 0000-0003-2604-0425, E-mail: zhaimengxi@pric.org.cn

that has remained stationary for at least 20 d. This duration is sufficient to preclude transient events such as drift ice being temporarily driven shoreward by oceanic or atmospheric forcing (Fraser, 2012).

In the Arctic Ocean, the maximum LFSI extent is 1.8×10^6 km^2 in winter (Yu et al., 2014), and accounts for approximately 13% of the surface area covered by sea ice in the Northern Hemisphere (Karvonen, 2018). LFSI appears repeatedly at the same locations at the same times of the year (Mahoney et al., 2018). It can move vertically due to tides or wind-driven sea level variations.

The local spatial distribution of LFSI is different in different coastal areas of the Arctic Ocean. The extent of LFSI, i.e., the distance from shoreline to the LFSI edge varies from several kilometers to several hundred kilometers, and depends largely on local bathymetry, slope of the continental shelf, and the topography of outlying islands (Leppäranta, 2011). Figure 1 shows LFSI distribution in the Arctic Ocean in April. The largest LFSI coverage is found in the Russian Arctic, including the

Kara, Laptev, and East Siberian seas, with winter LFSI edge extending to 300–500 km from the shore (Selyuzhenok et al., 2017). In the Chukchi and Beaufort seas, the typical LFSI extent is below 50 km associated with the relatively narrow shelf (Mahoney et al., 2014). In the Canadian Arctic Archipelago (CAA), LFSI fills the channels and straits, and favors the formation of ice bridges (Yu et al., 2014). Because of grounded icebergs and sea ice ridges on shallow shoals and banks, LFSI extent along the northeast coast of Greenland can reach up to 100 km (Hughes et al., 2011). Arctic LFSI is generally seasonal. It forms in autumn, reaches maximum extent in winter or spring, and decays from spring to summer. At maximum LFSI extent in winter, the ice edge is generally located between the 15 and 30 m isobaths (Divine et al., 2004; Mahoney et al., 2007; Selyuzhenok et al., 2015). Only in some locations in the CAA and sometimes in the Taymyr Peninsular region in Siberia, LFSI can survive through the summer because of geomorphological limitations.
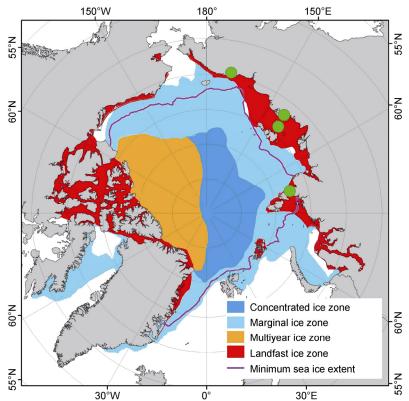

Figure 1 Distributions of different sea ice types in the Arctic Ocean. LFSI extent was derived from National Ice Center (NIC), USA, ice charts for the period of 1976–2018 (Li et al., 2020). Multiyear ice coverage (yellow), concentrated ice zone (blue) and marginal ice zone (light blue) are derived from National Snow and Ice Data Center (NSIDC), USA, ice concentration data for 1979–2011 (Strong and Rigor, 2013). Purple line represents the 1981–2010 average extent in September (acquired from NSIDC Sea Ice Index). Green dots are Russia LFSI stations (Kigilyakh, Ayon, Chelyuskin and Sannikova station).

Exchanges of material, energy and momentum between the atmosphere and the ocean are blocked by LFSI but can occur across coastal polynyas and flaw leads, which are often present at the LFSI edge. As a result, LFSI,

polynyas, and leads strongly influence regional ocean–ice–atmosphere interactions (Morales Maqueda, 2004; Fraser et al., 2019). In estuaries, large amounts of freshwater discharge affect LFSI formation; in the meantime, the

freezing-melting processes of LFSI affects local freshwater cycle and halocline stability owing to its large fresh water storage (Eicken et al., 2005; Itkin et al., 2015). Furthermore, fragmentation and subsequent northward advection of LFSI floes transport shelf-derived terrigenous materials into the deep basin, and even out of the Arctic Ocean (e.g., Krumpen et al., 2020). Fast ice plays an important role in the physics of the cryosphere but has yet to be integrated into global climate models.

Fast ice acts as a buffer zone and protects the coast from erosion by wave or drift ice (Rachold et al., 2000). Openings within the LFSI zone, e.g., cracks or leads, can be used by polar bears and seals to breed and feed, and can also be important habitats for birds, large vertebrates and microorganisms (Bluhm and Gradinger, 2008; Kooyman and Ponganis, 2014; Stauffer et al., 2014). Hence, LFSI is also a platform used by indigenous communities for fishing activities. Natural resources exploration is taking place in shallow coastal zones such as the Mackenzie Delta; construction of pipelines could promote local economic development (Solomon et al., 2008; Eicken et al., 2009). Fast ice also hinders the navigation of Arctic sea routes. The feasibility of Arctic shipping depends on the timing of LFSI breakup in key channels (Lei et al., 2015). Therefore, understanding of the annual cycle of LFSI is crucial for both scientific and economic purposes.

The number of LFSI studies has increased over the last two decades. These studies have focused on *in situ* and remote sensing observations, seasonality, interannual variability, thermodynamic and dynamic processes, and interactions with climate and ecosystems. In this paper, we provide an overview of the general features of Arctic LFSI, including spatiotemporal distribution, variations, key physical processes, and environmental implications. We summarize the results of the latest research on LFSI and propose future directions to promote LFSI research and improve our understanding of the role of Arctic LFSI in the climate system.

2   Characteristics of LFSI

2.1   Fasten mechanisms

Immobility is a fundamental characteristic of LFSI, which distinguishes LFSI from drift ice. Fast ice often appears repeatedly at the same locations at the same times of the year (Mahoney et al., 2018).   LFSI is generally a level and undeformed sea ice field adjoint with the shoreline. It either can grow outward from the shore or can be formed by the ice drifted to the shore. LFSI extent depends mainly on ice thickness, bathymetry and shoreline geometry. The four fasten mechanisms that anchor and stabilize (Figure 2) LFSI are summarized below.

(1) Bottom-fast ice grows in very shallow coastal zones with water depths of less than 2 m; it forms and thickens until it touches the seabed (Figure 2a) (Solomen et al., 2008). Its winter extent is in the order of kilometers. It is the most stable type of LFSI (Dammann et al., 2016). Unlike floating fast ice, bottom-fast ice does not oscillate with tides (Reimnitz, 2000). Tidal cracks may form at the boundary between the grounded and floating LFSI (Hui et al., 2016).

(2) Fast ice can also be stabilized by anchor points, such as islands, grounded ridges or icebergs (Figure 2b). Ice forms between anchor points that are close together and extends offshore. The minimum distance between anchor points required for LFSI to fasten depends on ice thickness. In some cases, grounded icebergs allow LFSI to extend into deep waters (Massom et al., 2003; Leppäranta, 2011). The ice can also be grounded and form stamukhi, especially at the LFSI edge.

(3) Fast ice can also be held in place by static arching of the ice between islands (Figure 2c; Olason, 2016). This mechanism is generally observed in narrow channels or straits, such as the tidal channel of Simpson Lagoon (Reimnitz, 2000). Goldstein et al. (2004) reported that the LFSI boundary in the Baltic Sea was formed of piecewise curved sections, or arches. Dumont et al. (2009) demonstrated the role of arching in the formation of an ice bridge in Nares Strait. Arch-like shapes have also been observed in the LFSI zone in the Laptev Sea (Haas et al., 2005; Selyuzhenok et al., 2015).

(4) Fast ice can be fastened to the upstream side of coastal protrusions (Fraser et al., 2012). The protrusions can be coastal promontories, islands, ice tongues or large tabular grounded icebergs. Newly formed ice is advected by coastal currents and blocked by the protrusions; this ice accumulates and attaches to the shore of the upstream side of the protrusion (Figure 2d).

2.2   Mass balance

LFSI mass balance is a fundamental research topic, and has been studied extensively in *in situ* observation and modeling studies.

2.2.1   Observations

Systematic long-term observations of LFSI thickness began in the Russian Arctic in the 1930s (Polyakov et al., 2003) and in the CAA in the 1950s (Brown and Cote, 1992; Howell et al., 2016). These observations were collected mostly by drilling through the ice at fixed stations. These data provide information on the seasonal evolution of ice thickness (Figure 3); ice growth rate, melt onset and evolution, and number of ice-free days can be derived and used to validate numerical models to study ice surface and bottom mass and energy balances. Figure 3 shows results from measurements that were made every 10 d. Autonomous measurement systems, e.g., ice mass balance buoys (IMBs), can also provide information on the seasonal evolution of LFSI with high temporal resolution (e.g., Wang et al, 2020).
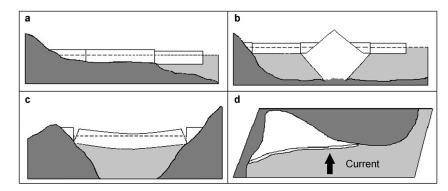
Figure 2 Schematic diagram showing how LFSI is fastened. **a**, bottom-fast ice; **b**, LFSI stabilized by anchor points; **c**, arching mechanism; **d**, advective regime.
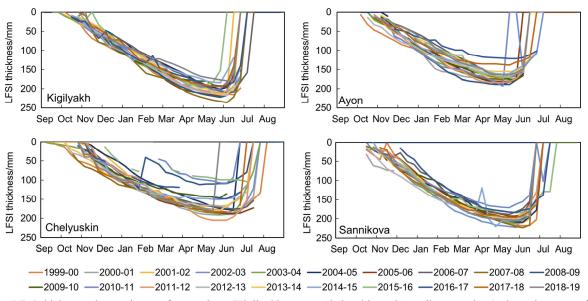

Figure 3 LFSI thickness observations at four stations (Kigilyakh, Ayon, Chelyuskin and Sannikova stations) along the coast of Russian Arctic in the past 20 years (see Figure 1 for positions).

In recent decades, many methods have been developed for the measurement of sea ice thickness, such as acoustic altimetry, IMBs, electromagnetic (EM) sounding, and satellite radar and laser altimetry. These approaches have been used to measure LFSI thickness as well. Fast ice thickness has been measured using downward-looking and upward-looking acoustic altimeters at Barrow, Alaska (Jones, 2016). Downward-looking altimeters above ice measure the freeboard of the snow or ice surface; upward-looking altimeter below ice measure ice draft; snow depth and ice thickness can be derived from the combined data. In addition to ice thickness, the IMB also measures the vertical profile of air, snow, ice, and upper ocean temperatures; from these measurements, information on the changes in the heat content of the snow-covered ice layer in response to atmospheric or oceanic heat sinks or sources can be derived for studies of LFSI thermodynamics (e.g., Wang et al., 2020). The EM system is towed below an aircraft and measures total snow and ice thickness (Haas et al., 2009). It has been used to measure the thickness of LFSI

in the Laptev Sea (Selyuzhenok, 2017) and off the northeast coast of Greenland (Wang et al., 2020). Long-term LFSI thickness has been retrieved from satellite data (e.g., Yu et al., 2014; Li et al., 2020). Using Cryosat-2 monthly Arctic sea ice thickness product, Li et al. (2020) estimated the interannual changes of LFSI between 2010 and 2018.

Outlying islands and a shallow ocean floor provide anchors for LFSI to stay in place and expand. As a result, the largest LFSI extents are found in these areas, e.g., in the coastal regions of Russia and the CAA. Over one third of the surface area of Arctic LFSI (6.6×10^5 km^2) is in the East Siberian, Laptev and Kara seas; here, the LFSI edge can extend up to 300 km offshore. Another third of the Arctic LFSI (5.4×10^5 km^2) is in the CAA (Yu et al., 2014; Mahoney, 2018; Li et al., 2020); here, LFSI forms nearshore initially, especially in the bays, channels, and shallow water around deltas or in other sheltered areas. Fast ice expands as a result of local thermal growth or formation of new ice drifted onshore. LFSI breakup occurs throughout the entire life cycle but mostly at the early formation and

late melting periods when the ice is thin or weak. Breakup may also happen in thick ice at the LFSI edge because of interactions with drift ice.

The remaining third of Arctic LFSI is spread along coasts with steep slopes and deep water that typically extend less than 50 km from the coast, e.g., the Chukchi and Beaufort seas (Mahoney, 2018). These coastlines are mostly open. Unlike the LFSI in shallow and sheltered shelves, LFSI in deep water largely forms through an accretionary process; ice formed elsewhere is transported into the coastal regions and becomes attached to the shoreline or seaward edge of existing LFSI (Reimnitz et al., 1978; Mahoney et al., 2007).

2.2.2 Thermodynamic models

Analytical models are a simple but valuable tool for the study of LFSI thermodynamics. Because of its simplified input and operation requirements, it can be easily used for auxiliary decision-making and interdisciplinary research related to LFSI. Leppäranta (1993) provides a clear overview of the elements of analytical sea ice thermodynamic models. First order LFSI growth is commonly estimated using the Stefan–Zubov's law (e.g., Yang et al., 2015), which assumes that the heat released from bottom ice growth is conducted to the ice surface following a constant temperature gradient and from the ice surface to the air following a fixed heat transfer coefficient; solar radiation, oceanic heat flux, and the influence of the snow cover are omitted. The ice thickness (h_i) is calculated as follows:

$$h_i = \sqrt{(h_0 + h')^2 + a^2 FDD} - h', \qquad (1)$$

where

$$a^2 = 2k_i / \rho_i L_i, \qquad (2)$$

$$FDD = \int_0^t (T_f - T_{sfc}) \mathrm{d}t, \qquad (3)$$

FDD is the accumulated freezing degree-days, T_f and T_{sfc} are the freezing point of sea water and sea surface air temperature, respectively. h_0 is the initial ice thickness, h' is ice–air heat transfer buffering thickness, t is time, and ρ_i, L_i and k_i are ice density, latent heat of fusion and thermal conductivity of ice, respectively. This model can be modified to include approximations of the influences of the oceanic heat flux and the snow cover (e.g., Lei et al., 2010).

Seasonal evolution of LFSI, especially the evolution of ice mass balance and snow–ice interactions, is mainly controlled by thermodynamic processes and can be fully described by numerical modeling (Maykut and Untersteiner, 1971; Flato and Brown, 1996; Cheng and Launiainen, 1998; Launiainen and Cheng, 1998; Shirasawa et al., 2006; Selyuzhenok et al., 2015). Figure 4 shows a schema of the

thermodynamic processes of LFSI. Ice mass balance is a result of the heat exchanges at the top and bottom boundaries. Fast ice thermodynamics are determined by atmospheric forcing (wind speed, air temperature, moisture, precipitation, and radiative fluxes), oceanic heat flux, and the physical properties of snow and sea ice (surface albedo, density, and heat conductivity). The surface heat balance over the ice can be given as:

$$(1 - \alpha_{i,s})Q_s - I(z)_0 + \varepsilon Q_d - Q_b(T_{sfc}) + Q_h(T_{sfc}) + \\ Q_{le}(T_{sfc}) + F_c(T_{sfc}) - F_m = 0 \qquad , \quad (4)$$

where Q_s represents the solar radiation, α is albedo of sea ice, $I(z)$ is the solar radiation penetrating below the surface snow/ice layer, Q_d and Q_b are incoming and outgoing longwave radiations, respectively, Q_h and Q_{le} are the sensible and latent heat fluxes, respectively, F_c is the conductive heat flux from below the surface, F_m represents surface melting. The surface temperature T_{sfc} can be derived from this equation.
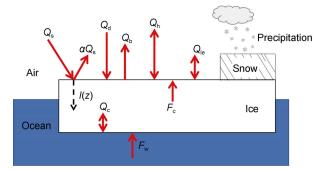

Figure 4 Schematically illustration of thermodynamic processes of LFSI in the vertical direction.

The snow and ice temperatures can be derived from the heat conduction equation:

$$(\rho c)_{i,s} \frac{\partial T_{i,s}(z,t)}{\partial t} = \frac{\partial}{\partial z}\left(k_{i,s} \frac{\partial T_{i,s}(z,t)}{\partial z} - q(z,t) \right), \quad (5)$$

where the subscripts s and i denote snow and ice, respectively, T is the temperature, t is time, and z is the vertical coordinate below the surface, ρ is density, c is specific heat, k is the thermal conductivity, and $q(z, t)$ is the absorbed solar radiation.

Because of the difference between snow (k_s) and ice (k_i) conductivities, heat conduction changes at the snow–ice interface, but the conductive heat flux between the snow and ice layers is continuous:

$$k_s \partial T_s / \partial z = k_i \partial T_i / \partial z, \qquad (6)$$

Freezing or melting at the bottom of the ice is determined by heat conduction $Q_c = \left(k_i \dfrac{\partial T_i}{\partial z} \right)$ and heat flux from the ocean (F_w):

$$\rho_i L_i \frac{dh_i}{dt} + F_w = \left(k_i \frac{\partial T_i}{\partial z} \right)_{bot} \tag{7}$$

Interaction between the snow and ice are not only limited to the heat conduction but also the phase transformation of snow to ice. In early winter when ice was thin, a heavy snow layer on top of the ice or local ice depression due to deformation may push the ice layer below ocean water surface and subsequently causing sea water flooding of the ice surface to form slush. A salty slush layer may freeze above the original ice cover to form snow ice (Leppäranta, 1983). Slush and snow ice may also form as a result of brine siphonage (Nicolaus et al., 2003). During the melt season, snow meltwater or rain may percolate downwards and refreeze above the original ice surface to form a layer of fresh meteoric ice defined as superimposed ice (Kawamura et al., 1997; Haas et al., 2001). These processes need to be included into LFSI thermodynamic models (Cheng et al., 2003; 2013) because snow ice and superimposed ice may be present in Arctic LFSI (Nicolaus et al., 2003, Wang et al., 2015). Snowmelt is also the main source of meltwater for melt ponds over LFSI, and the evolution of melt pond mainlyly relies on the roughness of

the snow or sea ice surface (Eicken et al., 2004; Grenfell and Perovich, 2004). In late spring, rain-on-snow events can accelerate the surface ablation of sea ice, thus greatly influencing the ice–albedo feedback (Dou et al., 2019, 2021). Observations of LFSI in Barrow, Alaska show that the reflection of LFSI decreased dramatically from 0.206 (close to bare ice) at the beginning of melt pond formation to 0.04 (close to seawater) when melt pond depth reached 10 cm (An et al., 2017). Thus, the timing of rain-on-snow events or seasonal change in the phase of precipitation from solid to liquid can be used as a reliable indicator to predict LFSI melt and breakup.

Most studies of Arctic LFSI have focused on the snow and ice mass balance using observations and models. Snow depth and LFSI thickness can be adequately estimated by numerical models (Flato and Brown, 1996; Cheng et al., 2013; Yang et al., 2015) because the seasonal changes in snow and LFSI thickness are mainly driven by thermodynamic processes (Yu et al., 2014). Figure 5 shows the simulated evolution of LFSI from a model that simulates the thermodynamic growth and decay of LFSI using meteorological parameters as inputs.
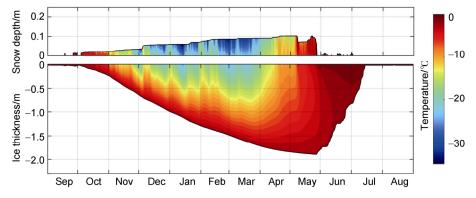

Figure 5   Modeled LFSI thickness and snow depth for year 2011/2012 at Kotelny Island, East Siberian Sea.

Because of the harsh polar environment, collection of *in situ* sea ice data remains a challenge. Therefore, remote sensing data have been used to study the features of Arctic sea ice, especially over large scales. However, the accuracy of LFSI thickness retrieved from remote sensing data is low. Thermodynamic modeling can be used to fill the gaps in remote sensing data. The seasonal cycle of ice mass balance and some dynamic feature of LFSI can be studied by combining remote sensing data and thermodynamic modeling (e.g., Zhai et al., 2021).

3   Dynamics of LFSI

3.1   Dynamic features of LFSI

The initial formation of LFSI involves many oceanic dynamic processes, such as the cooling and mixing of coastal seawater. Once the LFSI is formed and consolidated,

there is little horizontal motion in most of the ice. However, occasional displacements occur because of various dynamic processes (Figure 6). At the LFSI edge, interactions with drift ice floes can result in dynamic processes, such as ridging, rafting, fracturing, and shearing in the outer zone. In the melt season, the contact between the LFSI and the coast loosens and allows more ice motion. In addition, waves penetrating the LFSI zone may break the ice, even generating a drift-ice-like ice floe field (Petrich et al., 2012). In shallow water, ice ridges can ground to form stamukhi, which can shield and reinforce the expansion of the LFSI (Fraser et al., 2012).

3.2   Methods used to investigate LFSI dynamics

Landfast ice dynamics have been studied using professional camera or webcam systems and land-based marine radars. At Barrow, Alaska, a webcam was used to record sea ice conditions during the melt season (Petrich et al., 2012).

Low visibility and frost on the camera lens are the major technical bottlenecks, which can be overcome by the use of
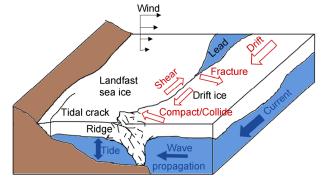

Figure 6 Schematic illustration of various dynamics processes of the LFSI. Red arrows show the possible dynamic processes, i.e., shearing, fracturing, compacting/collision at the LFSI edge. Grounding of ridges can occur. The LFSI can be affected by various oceanic dynamical forces, such as waves propagation, tides, and currents. Thermal cracks jointly with tidal cracks can form close to the shore.

a land-based marine radar. Various parameters, including ice extent, surface morphological features, and potential displacement of LFSI can be derived from the

backscattering of radar signals from the sea ice surface (Jones, 2016). For example, it is possible to identify grounded ridges, LFSI edge, and melt ponds in both marine radar images and camera images that were captured under good weather conditions. The camera has a higher spatial resolution and the marine radar has a higher spatial coverage. They can be used together to monitor LFSI development and evolution and nearshore sea ice dynamics.

Satellite images are widely used to detect LFSI dynamics along the Arctic coast. Fast ice edges are clearly visible from SAR imagery, e.g., Envisat (ASAR) and Sentinel-1 SAR imagery, during the cold season and under all weather conditions (Meyer et al., 2011; Mahoney et al., 2014). They are also visible from optical imagery, e.g., Aqua/Terra (MODIS) and Landsat-8, during the seasons with sun and under clear skies (Fraser et al., 2010). In recent years, SAR interferometry (InSAR) has been used to evaluate LFSI stability (Dammert et al., 1998; Marbouti et al., 2017; Dammann et al., 2019) and deformation (divergence, rotation and shear) (Dammann et al., 2016). Furthermore, fasten mechanisms, such as grounded ridges (Figure 7d) or bottom-fast ice can be identified using InSAR technique (Dammann et al., 2018). Figure 7 shows a few examples of LFSI dynamics. Ridges, flaw leads, LFSI
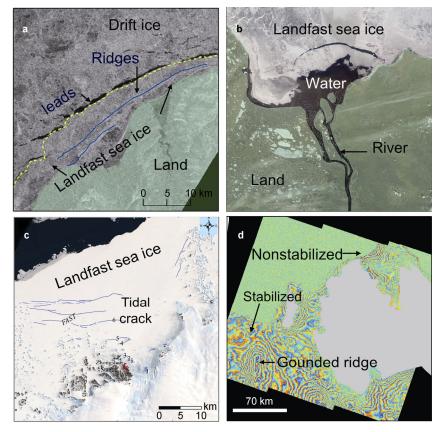

Figure 7 Satellite images showing LFSI features and stability. **a**, Envisat ASAR image showing LFSI features – ice types, leads and ridges (Zhai et al., 2021); **b**, MODIS image showing clearly the LFSI and river outflow in high Arctic Russia coast during early summer; **c**, Landsat-8 image showing tidal cracks in LFSI (Hui et al., 2016); **d**, Interferometric phase fringes from Sentinel-1 images showing small deformation of LFSI and identifying its stability.

and drift ice can be clearly seen (Figures 7a, 7b and 7c). Tidal cracks can be identified in Figure 7c. Fringes in the interferometry image derived from consecutive Sentinel SAR images can be used to assess LFSI stability.

Fast ice dynamics have also been studied using models. König Beatty and Holland (2010) simulated LFSI in the Kara Sea by adding tensile strength to two versions of the elastic–viscous–plastic sea ice rheology as well as to the viscous–plastic rheology; only idealized one-dimensional cases were examined. Olason (2016) used a maximum viscosity that was above the standard value and a solver for the momentum equation to solve for small ice velocities. Using a parametrization that involved bathymetry, LFSI thickness and the mechanism of ice anchoring, Lemieux et al. (2015) introduced grounded ridges into a classical sea ice model. To model the LFSI in the Siberian Seas, Itkin et al. (2015) designed a parameterization based on König Beatty and Holland (2010) to take into account tensile strength and water depth.

3.3   Freeze-up

The beginning of the LFSI season is controlled by both thermodynamic and mechanical processes (Leppäranta, 2013; Selyuzhenok et al., 2015). Dynamic processes, such

as ice rafting, ridging, and piling up may take place prior to ice consolidation. Using consecutive remote sensing images and thermodynamic modeling, Zhai et al. (2021) examined the LFSI in the East Siberian Sea; Figure 8 shows successive ASAR images of LFSI during the freezing season along the northwest coast of Kotelny Island in the East Siberian Sea; the newly formed ice (20 October, 2 and 4 November in Figure 8) is unstable. Results from the thermodynamic model suggest that stabilization begins when level ice thickness reaches 0.3 m; ASAR images show that stabilization occurs when ice thickness reaches 0.3–0.6 m (11, 15 and 24 November in Figure 8). When ice thickness exceeds 0.6 m, the ice becomes stable and immobile, and cannot be easily destroyed by winds or tides. Karklin et al. (2013) used an ice thickness of 0.05–0.1 m to denote the onset of LFSI formation in the Laptev Sea. This definition is different from that used at regional or the pan-Arctic scales. The onset of LFSI formation on a large scale is generally defined by a threshold of LFSI area (Yu et al., 2014; Selyuzhenok et al., 2015) or width (Mahoney et al., 2014). However, application of these thresholds is limited because revisit times preclude the use of consecutive satellite images.
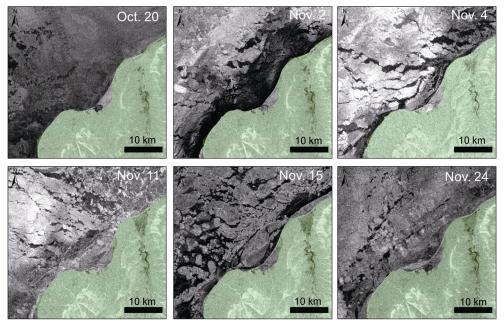

Figure 8   Envisat ASAR imagery showing LFSI freeze-up process. Images are acquired from 20 October to 24 November for ice season 2007/2008 northwest coast of Kotelny Island, East Siberian Sea.

3.4   Breakup

Melting and dynamic fracturing are the main mechanisms resulting in LFSI breakup. In the satellite image in Figure 9, dynamic fracturing can be clearly seen near the LFSI edge (left panel), whereas melting occurred throughout the whole LFSI area (right panel).

The relative dominance of dynamic and thermodynamic

processes varies with location. In the Laptev Sea, the LFSI cover thins by melting until it detaches from the coast and is disintegrated by winds, currents, or waves (Petrich et al., 2012). In the CAA region, the LFSI is confined by islands. Therefore, breakup is dominated by melting (Melling, 2002), and results in a relatively consistent breakup onset time each year (Galley et al., 2012). In the Chukchi Sea, the LFSI is located along the coastline and is unrestricted by
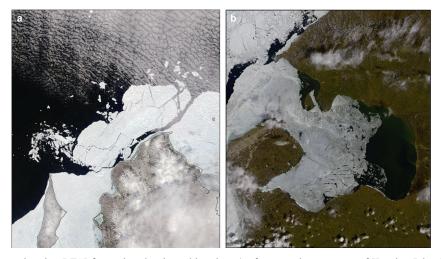
Figure 9 MODIS images showing LFSI fracturing dominated breakup (**a**, from northwest coast of Kotelny Island, East Siberian Sea) and melting dominated breakup (**b**, at the Chaunskaya Bay, East Siberian Sea).

islands; there is a correlation between breakup onset and the cumulative amount of solar radiation absorbed by the surface (Petrich et al., 2012). However, for firmly anchored LFSI (Figure 2b), breakup onset is more likely to be controlled by the occurrence of strong winds or currents and changes in local sea level (Divine et al., 2004; Mahoney et al., 2007; Jones et al., 2016). Near major rivers, the breakup of LFSI can be triggered by spring river discharge (Divine et al., 2003). For LFSI in estuaries, river outflow brings freshwater that influences the halocline and results in early spring melt (Selyuzhenok et al., 2015).

4 Spatial and temporal distributions of LFSI

Although LFSI is largely immobile, the atmosphere and ocean can still cause large spatial, temporal and regional variations of Arctic LFSI.

4.1 Extent

Fast ice extent has been changing at different rates across the Arctic. The ice charts from the Arctic and Antarctic Research Institute (AARI) in Russia show no consistent trend in maximum LFSI extent in the Laptev Sea between 1999 and 2013 (Selyuzhenok et al., 2015). However, sea ice charts and satellite images show that LFSI extent in the Kara Sea has decreased by approximately 12% between 1953 and 1990 (Divine et al., 2003). The largest decrease in LFSI extent is found in the northern waters of the CAA between 1976 and 2007 (Yu et al., 2014). In the Chukchi Sea, the annual maximum width of LFSI has reduced by an average of 13 km (approximately 50%) between 1973–1976 (Stringer, 1978) and 1996–2008 (Mahoney et al., 2014). However, there has been little variation in the annual maximum width of the LFSI in the Beaufort Sea between 1973–1976 and 1996–2008. Using seasonal average LFSI extent data between January and May from the NIC weekly

ice charts, Yu et al. (2014) found that overall Arctic LFSI extent decreased between 1976 and 2007 at a rate of $(12.3\pm2.8)\times10^3$ km$^2\cdot$a^{-1} (7% per year). Between 1976 and 2018, LFSI extent decreased at an average rate of $(1.1\pm0.5)\times10^4$ km$^2\cdot$a^{-1} (10.5% per decade), while all Arctic sea ice decreased at a rate of $(6.0\pm2.4)\times10^4$ km$^2\cdot$a^{-1} (5.2% per decade) (Li et al., 2020).

4.2 Thickness

First year Arctic sea ice can grow thermodynamically to a thickness of approximately 2 m (Leppäranta, 1993). As a rule of thumb, this is the case for Arctic LFSI. However, LFSI has been thinning over the past decades because of climate change. Polyakov et al. (2012) reported that the LFSI thickness on the Siberian coast has decreased by approximately 0.3 m since the 1990s. Between 1936 and 2000, LFSI thickness decreased at an average rate of approximately 1 cm$\cdot$(10 a)$^{-1}$ (Polyakov, 2003). The highest rate of LFSI thickness decrease between 1976 and 2018 is found in the northern CAA; ice thickness, which often exceeds 2.5 m, decreased by 0.1 m$\cdot$a^{-1} (Li et al., 2020). According to Howell et al. (2016), the maximum LFSI thickness has reduced by about 0.25 m (approximately 10%) in most areas of the CAA. In the Chukchi Sea, the annual maximum LFSI thickness around Utqiaġvik, Alaska decreased by approximately 0.30 m between 2000 and 2016 (Eicken et al., 2012). Between 1966 and 2007, LFSI thickness at Hopen in the Barents Sea decreased at a rate of 1 cm$\cdot$a^{-1} (Gerland et al., 2008).

4.3 Season length

The majority of Arctic LFSI is seasonal ice. The annual length of the LFSI season is 7–9 months. In some locations, e.g., in the CAA, the LFSI can survive for a few years. However, similar to the season length of all Arctic sea ice, the season length of LFSI has also decreased considerably. Selyuzhenok et al. (2015) examined AARI ice charts

between 1999 and 2013 and reported a decrease of approximately 3 d·a^{-1} in the season length of LFSI in the Laptev Sea and a decrease of up to 7 weeks per decade in the southeastern Laptev Sea. The LFSI season has become shorter in all parts of the CAA (Galley et al., 2012). Canadian Ice Service (CIS) charts between 1980 and 2009 show that the season length of Arctic LFSI decreased by 1–3 weeks per decade in most regions. The decrease rate was 2–5 weeks per decade in the Viscount Melville Sound, the western part of M'Clure Strait and the Gulf of Boothia, and 7–10 weeks per decade in the northern Queen Elizabeth Islands, the Robeson Channel, and the northeastern part of Smith Sound. Between 1973–1977 (Barry et al., 1979) and 1996–2008 (Mahoney et al., 2014), LFSI season length in the western Beaufort Sea and the Chukchi Sea decreased by 53 d (~2 d·a^{-1}) and 38 d (~1.4 d·a^{-1}), respectively. The reduced length of the LFSI season is also likely to be a strong driver for the reduced LFSI thickness at the end of winter.

5　Environmental impacts

In the shallow waters of the East Siberian shelf, methane released from the coastal permafrost below seabed rises to the surface and enters the atmosphere (Shakhova et al., 2015) or is transported to the central Arctic Ocean by the transpolar current (Damm et al., 2018). The growth and ablation of LFSI along the coast affect local freshwater circulation and the stability of the halocline (Eicken et al., 2005; Itkin et al., 2015). The decrease of LFSI thickness and the advance of spring melting increase the accumulation of solar shortwave radiation in the ocean. Consequently, higher summer water temperature promotes the melting of seabed permafrost and release of methane and delays LFSI freeze-up in autumn. In spring, polynyas and leads may promote sea ice retreat by enhancing the positive ice–albedo feedback and the dynamic breakup of sea ice. The rapid retreat of drift ice northward in the early summer may increase cyclone activity (Kapsch et al., 2019), enhance wave and/or swell, increase dynamic forcing, and cause rapid fragmentation of the LFSI.

There have been studies of Arctic LFSI focusing on the associated environmental implications and on the cryosphere. Arctic warming and sea ice retreat of LFSI trigger coastal erosion. Thinner LFSI can increase the accumulation of solar radiation in the ocean and favor local climates that contribute to further Arctic warming. Moreover, early melting of sea ice favors phytoplankton growth, which leads to earlier algae blooms (Kahru et al., 2016). Local human communities need to adapt their ways of life because the ice cover has become less safe as a platform. Climate models also need to take LFSI into consideration. Landfast ice breakup and the subsequent ice drift along the coast remain to be investigated. Terrestrial particles can be transported by fragments of former LFSI

away from the coast. Broken ice floes and icebergs are potential hazards for coastal shipping. The extent and duration of the contact between grounded LFSI and the sediment bed determine the total winter heat loss from the ground and the spatial distribution and depth of seasonal frost (Stevens et al., 2010).

Dmitrenko et al. (2010) and Qin et al. (2019) reported that the LFSI in the coastal areas of the Laptev and the East Siberian seas are closely associated with river runoff. Late autumn runoff alters the salinity of coastal water and changes the freezing temperature (Eicken et al., 2005). Winter runoff has the potential to shape and modify the LFSI edge (Dmitrenko et al., 1999). Spring runoff enhances LFSI breakup (Bareiss et al., 1999).

Fast ice is a stable platform. Local communities benefit from ice roads built on fast ice. These roads can be used for commercial transportation and recreational activities such as skiing and ice fishing. Various countries have developed LFSI information services. The CIS produces ice charts and remote sensing products for the CAA region (Trishchenko and Luo, 2021). Others include the BALFI system (Mäkynen et al., 2020) for Baltic Sea and Fast Ice Prediction System (FIPS) for Prydz Bay, East Antarctica (Zhao et al., 2020).

6　Conclusions and perspectives

In this paper, we reviewed the physics of Arctic LFSI and associated implications on the cryosphere. Arctic LFSI varies with the location. Around southeast Greenland and Svalbard and along the Barents Sea coast, the LFSI season is relatively short and annual maximum ice thickness remains below 1 m. In the coastal regions between the Kara and the East Siberian seas, the LFSI season is relatively long and annual maximum ice thickness and extent are large. In the coastal regions between the Chukchi and Beaufort seas, the LFSI is similar to that in the second category but has a smaller annual maximum extent because of the narrow continental shelf. In the straits around the CAA and northern Greenland, the LFSI is subject to weak dynamic influence; its season length is potentially the longest.

Many studies have suggested that, consistent with the trends of all Arctic sea ice, the season length, thickness and extent of Arctic LFSI are decreasing. Declines in extent and thickness in LFSI are smaller than those in all Arctic sea ice. These results suggest that decline in Arctic sea ice is mostly occurring in the drift ice zone. However, the relative extent loss (i.e., the ratio between decrease in extent and total extent) in the LFSI zone is larger than that of all Arctic sea ice. These results indicate that the LFSI zone may be ice-free for longer durations in the future.

To improve our understanding of LFSI, both *in situ* observations and modeling studies are needed. Enhanced field research efforts will improve our scientific understanding and also allow local communities to better

identify vulnerabilities and develop adaptation plans (Furgal and Seguin, 2006). Local changes in LFSI have been recorded by different local communities over generations. Because languages and methodologies differ between communities these historical records need to be standardized. They can be valuable to the operators of nearshore oil and gas platforms in the Arctic (Dammann et al., 2018). Landfast ice connects the Arctic terrestrial, marine and atmospheric environments. Field studies of LFSI can improve our understanding of the environmental interactions across various spheres in a changing Arctic. Observations of LFSI at the seasonal and interannual scales have been crucial to LFSI model development (Lemieux et al., 2015; Olason, 2016).

To meet future needs, a monitoring strategy similar to the one proposed for Antarctic LFSI (Heil et al., 2011) is needed for Arctic LFSI. The strategy needs to include measurements of LFSI extent and thickness and provide information on the LFSI annual cycle. Community-based monitoring offers a means of collecting high quality *in situ* observations (Mahoney et al., 2009; Eicken et al., 2014), but co-production of knowledge (Behe and Daniel, 2018) at early stages of research design can help to ensure a sound strategy that will generate information of value for all stakeholders. Landfast ice monitoring is currently conducted by individual countries or stations at various locations. A unified and systematic Arctic LFSI observation network is needed. To maintain a large continuous monitoring network, local indigenous communities will need to be involved.

Remote sensing, unmanned aerial vehicle and shore-based radar observations provide useful information, in particular for the monitoring of LFSI freeze-up and breakup. Data from InSAR data can be used to detect small-scale ice motion and map LFSI stability and interactions between LFSI, river ice, and drift ice. We need to develop an automated approach to measure LFSI extent (Mahoney et al., 2018). In recent years, SAR images have been used in the study of LFSI (Dammann et al., 2018, 2019) which may improve the accuracy of extent statistics in future. The modelling of LFSI have been mainly focused on thermodynamics. Dynamics modeling of landfast ice has not drawn much attention in the sea ice modeling community. Most sea ice models are unable to reproduce LFSI dynamics in a realistic setting (Olason, 2016). Further studies are therefore needed. Extensive international cooperation including *in situ* observations, satellite remote sensing data and/or numerical simulations, is needed in the study of Arctic LFSI.

In this review, we have mainly focused on Arctic LFSI studies. The LFSI in the Antarctic and subarctic seas are equally important and have been examined by numerous studies conducted by various national or international programs, including Chinese National Antarctic Research Expedition (Lei et al., 2010; Zhao et al., 2020) and Antarctica Fast Ice Network (Heil et al., 2011).

References

An H M, Dou T F, Che T, et al. 2017. Measurements of the surface features and the reflectance of Arctic Sea ice during the initial phase of the melt season in Barrow. J Glaciol Geocryol, 39(1): 35-42, doi: 10.7522/j.issn.1000-0240.2017.0005 (in Chinese with English abstract).

Bareiss J, Eicken H, Helbig A, et al. 1999. Impact of river discharge and regional climatology on the decay of sea ice in the Laptev Sea during spring and early summer. Arct Antarct Alp Res, 31(3): 214-229, doi:10.1080/15230430.1999.12003302.

Barry R G, Moritz R E, Rogers J C. 1979. The fast ice regimes of the Beaufort and Chukchi Sea coasts, Alaska. Cold Reg Sci Technol, 1(2): 129-152, doi:10.1016/0165-232X(79)90006-5.

Behe C, Daniel R, Richter-Menge J, et al. 2018. Indigenous knowledge and the coproduction of knowledge process: Creating a holistic understanding of Arctic change. State of the Climate in 2017, 99(8): 160.

Bluhm B A, Gradinger R. 2008. Regional variability in food availability for Arctic marine mammals. Ecol Appl, 18(sp2): S77-S96, doi:10.1890/06-0562.1.

Brown R D, Cote P. 1992. Interannual variability of landfast ice thickness in the Canadian High Arctic, 1950-89. Arctic, 45(3): 273-284, doi:10.14430/arctic1402.

Cheng B, Launiainen J. 1998. A one-dimensional thermodynamic air-ice-water model: technical and algorithm description report. MERI, 37: 15-36.

Cheng B, Mäkynen M, Similä M, et al. 2013. Modelling snow and ice thickness in the coastal Kara Sea, Russian Arctic. Ann Glaciol, 54(62): 105-113, doi:10.3189/2013aog62a180.

Cheng B, Vihma T, Launiainen J. 2003. Modelling of superimposed ice formation and subsurface melting in the Baltic Sea. Geophysica, 39: 31-50.

Damm E, Bauch D, Krumpen T, et al. 2018. The Transpolar Drift conveys methane from the Siberian Shelf to the central Arctic Ocean. Sci Rep, 8(1): 4515, doi:10.1038/s41598-018-22801-z.

Dammann D O, Eicken H, Mahoney A R, et al. 2018. Evaluating landfast sea ice stress and fracture in support of operations on sea ice using SAR interferometry. Cold Reg Sci Technol, 149: 51-64, doi:10.1016/j.coldregions.2018.02.001.

Dammann D O, Eicken H, Meyer F J, et al. 2016. Assessing small-scale deformation and stability of landfast sea ice on seasonal timescales through L-band SAR interferometry and inverse modeling. Remote Sens Environ, 187: 492-504, doi:10.1016/j.rse.2016.10.032.

Dammann D O, Eriksson L E B, Mahoney A R, et al. 2019. Mapping pan-Arctic landfast sea ice stability using Sentinel-1 interferometry. Cryosphere, 13(2): 557-577, doi:10.5194/tc-13-557-2019.

Dammert P B G, Lepparanta M, Askne J. 1998. SAR interferometry over

Baltic Sea ice. Int J Remote Sens, 19(16): 3019-3037, doi:10.1080/014311698214163.

Divine D, Korsnes R, Makshtas A. 2003. Variability and climate sensitivity of fast ice extent in the north-eastern Kara Sea. Polar Res, 22(1): 27-34, doi:10.3402/polar.v22i1.6440.

Divine D, Korsnes R, Makshtas A. 2004. Temporal and spatial variation of shore-fast ice in the Kara Sea. Cont Shelf Res, 24(15): 1717-1736, doi:10.1016/j.csr.2004.05.010.

Dmitrenko I A, Golovin P N, Gribanov V A, et al. 1999. The influence of river runoff on the formation of hydrological and ice conditions on the Russian Arctic Shelf. Dokl Earth Sci, 369: 1372-1376.

Dmitrenko I A, Kirillov S A, Krumpen T, et al. 2010. Wind-driven diversion of summer river runoff preconditions the Laptev Sea coastal polynya hydrography: evidence from summer-to-winter hydrographic records of 2007–2009. Cont Shelf Res, 30(15): 1656-1664, doi:10.1016/j.csr.2010.06.012.

Dou T, Xiao C, Liu J, et al. 2019. A key factor initiating surface ablation of Arctic sea ice: earlier and increasing liquid precipitation. Cryosphere, 13(4): 1233-1246, doi:10.5194/tc-13-1233-2019.

Dou T, Xiao C, Liu J, et al. 2021. Trends and spatial variation in rain-on-snow events over the Arctic Ocean during the early melt season. Cryosphere, 15: 883-895, doi:10.5194/tc-15-883-2021.

Druckenmiller M L, Eicken H, George J C, et al. 2010. Assessing the shorefast ice: iñupiat whaling trails off barrow, Alaska. SIKU: Knowing Our Ice. Dordrecht: Springer Netherlands, 203-228, doi:10.1007/978-90-481-8587-0_9.

Dumont D, Gratton Y, Arbetter T E. 2009. Modeling the dynamics of the North Water Polynya ice bridge. J Phys Oceanogr, 39(6): 1448-1461, doi:10.1175/2008jpo3965.1.

Eicken H, Dmitrenko I, Tyshko K, et al. 2005. Zonation of the Laptev Sea landfast ice cover and its importance in a frozen estuary. Glob Planet Change, 48(1-3): 55-83, doi:10.1016/j.gloplacha.2004.12.005.

Eicken H, Gradinger R, Heinrichs T, et al. 2012. Automated ice mass balance data (SIZONET). NSF Arctic Data Center.

Eicken H, Grenfell T C, Perovich D K, et al. 2004. Hydraulic controls of summer Arctic pack ice albedo. J Geophys Res Oceans, 109(C8): C08007, doi:10.1029/2003JC001989.

Eicken H, Kaufman M, Krupnik I, et al. 2014. A framework and database for community sea ice observations in a changing Arctic: an Alaskan prototype for multiple users. Polar Geogr, 37(1): 5-27, doi:10.1080/1088937X.2013.873090.

Eicken H, Lovecraft A L, Druckenmiller M L. 2009. Sea-ice system services: a framework to help identify and meet information needs relevant for observing networks. ARCTIC, 62(2): 119-136, doi:10.14430/arctic126.

Flato G M, Brown R D. 1996. Variability and climate sensitivity of landfast Arctic sea ice. J Geophys Res Oceans, 101(C11): 25767-25777, doi:10.1029/96JC02431.

Ford J D, Clark D, Pearce T, et al. 2019. Changing access to ice, land and water in Arctic communities. Nat Clim Change, 9(4): 335-339, doi:10.1038/s41558-019-0435-7.

Ford J D, Gough W A, Laidler G J, et al. 2009. Sea ice, climate change, and community vulnerability in northern Foxe Basin, Canada. Clim Res, 38: 137-154, doi:10.3354/cr00777.

Fraser A D, Massom R A, Michael K J. 2010. Generation of high-resolution East Antarctic landfast sea-ice maps from cloud-free

MODIS satellite composite imagery. Remote Sens Environ, 114(12): 2888-2896, doi:10.1016/j.rse.2010.07.006.

Fraser A D, Massom R A, Michael K J, et al. 2012. East Antarctic landfast sea ice distribution and variability, 2000–08. J Clim, 25(4): 1137-1156, doi:10.1175/jcli-d-10-05032.1.

Fraser A D, Ohshima K I, Nihashi S, et al. 2019. Landfast ice controls on sea-ice production in the Cape Darnley Polynya: a case study. Remote Sens Environ, 233: 111315, doi:10.1016/j.rse.2019.111315.

Furgal C, Seguin J. 2006. Climate change, health, and vulnerability in Canadian northern Aboriginal communities. Environ Health Perspect, 114(12): 1964-1970, doi:10.1289/ehp.8433.

Galley R J, Else B G T, Howell S E L, et al. 2012. Landfast Sea ice conditions in the Canadian Arctic: 1983–2009. Arctic, 65(2): 133-144, doi:10.14430/arctic4195.

Gerland S, Renner A H H, Godtliebsen F, et al. 2008. Decrease of sea ice thickness at Hopen, Barents Sea, during 1966–2007. Geophys Res Lett, 35(6): L06501, doi:10.1029/2007GL032716.

Goldstein R V, Osipenko N N, Leppäranta M, et al. 2004. On the shape of the fast ice-drift ice contact zone. Geophysica, 40(1-2): 3-13.

Grenfell T C, Perovich D K. 2004. Seasonal and spatial evolution of albedo in a snow-ice-land-ocean environment. J Geophys Res Oceans, 109(C1): C01001, doi:10.1029/2003JC001866.

Haas C. 2001. The seasonal cycle of ERS scatterometer signatures over perennial Antarctic sea ice and associated surface ice properties and processes. Ann Glaciol, 33: 69-73, doi:10.3189/172756401781818301.

Haas C, Dierking W, Busche T, et al. 2005. Envisat ASAR monitoring of polynya processes and sea ice production in the Laptev Sea. Salzburg: Proceedings, ESA Envisat Symposium.

Haas C, Lobach J, Hendricks S, et al. 2009. Helicopter-borne measurements of sea ice thickness, using a small and lightweight, digital EM system. J Appl Geophys, 67(3): 234-241, doi:10.1016/j.jappgeo.2008.05.005.

Heil P, Gerland S, Granskog M A. 2011. An Antarctic monitoring initiative for fast ice and comparison with the Arctic. Cryosphere Discuss, 5(5): 2437-2463, doi:10.5194/tcd-5-2437-2011.

Howell S E L, Laliberté F, Kwok R, et al. 2016. Landfast ice thickness in the Canadian Arctic Archipelago from observations and models. Cryosphere, 10(4): 1463-1475, doi:10.5194/tc-10-1463-2016.

Hughes N E, Wilkinson J P, Wadhams P. 2011. Multi-satellite sensor analysis of fast-ice development in the Norske Øer Ice Barrier, northeast Greenland. Ann Glaciol, 52(57): 151-160, doi:10.3189/172756411795931633.

Hui F, Li X, Zhao T, et al. 2016. Semi-automatic mapping of tidal cracks in the fast ice region near Zhongshan Station in East Antarctica using landsat-8 OLI imagery. Remote Sens, 8(3): 242, doi:10.3390/rs8030242.

Itkin P, Losch M, Gerdes R. 2015. Landfast ice affects the stability of the Arctic halocline: evidence from a numerical model. J Geophys Res Oceans, 120(4): 2622-2635, doi:10.1002/2014JC010353.

Jones J, Eicken H, Mahoney A, et al. 2016. Landfast sea ice breakouts: Stabilizing ice features, oceanic and atmospheric forcing at Barrow, Alaska. Cont Shelf Res, 126: 50-63, doi:10.1016/j.csr.2016.07.015.

Kahru M, Lee Z P, Mitchell B G, et al. 2016. Effects of sea ice cover on satellite-detected primary production in the Arctic Ocean. Biol Lett, 12(11): 20160223, doi:10.1098/rsbl.2016.0223.

Kapsch M L, Skific N, Graversen R G, et al. 2019. Summers with low Arctic sea ice linked to persistence of spring atmospheric circulation patterns. Clim Dyn, 52(3): 2497-2512, doi:10.1007/s00382-018-4279-z.

Karklin V, Karelin I, Julin A, et al. 2013. Osobennosti formirovanija pripaja v more Laptevyh. Peculiarities of landfast ice formation in the Laptev Sea. Problemy Arktiki i Antarctiki, 3: 5-13.

Karvonen J. 2018. Estimation of Arctic land-fast ice cover based on dual-polarized Sentinel-1 SAR imagery. Cryosphere, 12(8): 2595-2607, doi:10.5194/tc-12-2595-2018.

König Beatty C, Holland D M. 2010. Modeling landfast sea ice by adding tensile strength. J Phys Oceanogr, 40(1): 185-198, doi:10.1175/2009jpo4105.1.

Kooyman G L, Ponganis P J. 2014. Chick production at the largest emperor penguin colony decreases by 50% from 2008–10. Antarct Sci, 26(1): 33-37, doi:10.1017/s0954102013000515.

Krumpen T, Birrien F, Kauker F, et al. 2020. The MOSAiC ice floe: sediment-laden survivor from the Siberian shelf. Cryosphere, 14(7): 2173-2187, doi:10.5194/tc-14-2173-2020.

Kwok R. 2018. Arctic sea ice thickness, volume, and multiyear ice coverage: losses and coupled variability (1958–2018). Environ Res Lett, 13(10): 105005, doi:10.1088/1748-9326/aae3ec.

Laidler G J, Ford J D, Gough W A, et al. 2009. Travelling and hunting in a changing Arctic: assessing Inuit vulnerability to sea ice change in Igloolik, Nunavut. Clim Change, 94(3-4): 363-397, doi:10.1007/s10584-008-9512-z.

Launiainen J, Cheng B. 1998. Modelling of ice thermodynamics in natural water bodies. Cold Reg Sci Technol, 27(3): 153-178, doi:10.1016/S0165-232X(98)00009-3.

Lei R, Li Z, Cheng B, et al. 2010. Annual cycle of landfast sea ice in Prydz Bay, East Antarctica. J Geophys Res Oceans, 115(C2): C02006, doi:10.1029/2008jc005223.

Lei R, Xie H, Wang J, et al. 2015. Changes in sea ice conditions along the Arctic Northeast Passage from 1979 to 2012. Cold Reg Sci Technol, 119: 132-144, doi:10.1016/j.coldregions.2015.08.004.

Lemieux J F, Tremblay L B, Dupont F, et al. 2015. A basal stress parameterization for modeling landfast ice. J Geophys Res Oceans, 120(4): 3157-3173, doi:10.1002/2014JC010678.

Leppäranta M. 1983. A growth model for black ice, snow ice and snow thickness in subarctic basins. Hydrol Res, 14(2): 59-70, doi:10.2166/nh.1983.0006.

Leppäranta M. 1993. A review of analytical models of sea-ice growth. Atmosphere-Ocean, 31(1): 123-138, doi:10.1080/07055900.1993.9649465.

Leppäranta M. 2011. The drift of sea ice. 2nd Edn. Heidelberg, Germany: Springer-Praxis.

Leppäranta M. 2013. Land-ice interaction in the Baltic Sea. Estonian J Earth Sci, 62(1): 2-14, doi:10.3176/earth.2013.01.

Li Z, Zhao J, Su J, et al. 2020. Spatial and temporal variations in the extent and thickness of Arctic landfast ice. Remote Sens, 12(1): 64, doi:10.3390/rs12010064.

Lu P, Li Z, Zhang Z, et al. 2008. Aerial observations of floe size distribution in the marginal ice zone of summer Prydz Bay. J Geophys Res Oceans, 113(C2): C02011, doi:10.1029/2006JC003965.

Mahoney A. 2018. Landfast sea ice in a changing Arctic. Arctic Report Card 2018, 99.

Mahoney A, Eicken H, Gaylord A G, et al. 2007. Alaska landfast sea ice: links with bathymetry and atmospheric circulation. J Geophys Res Oceans, 112(C2): C02001, doi:10.1029/2006JC003559.

Mahoney A, Gearheard S, Oshima T, et al. 2009. Sea ice thickness measurements from a community-based observing network. Bull Amer Meteor Soc, 90(3): 370-378, doi:10.1175/2008bams2696.1.

Mahoney A R, Eicken H, Gaylord A G, et al. 2014. Landfast sea ice extent in the Chukchi and Beaufort seas: the annual cycle and decadal variability. Cold Reg Sci Technol, 103: 41-56, doi:10.1016/j.coldregions.2014.03.003.

Mahoney A, Eicken H, Shapiro L, Graves A. 2005. Defining and locating the seaward landfast ice edge in northern Alaska. Potsdam, New York: 18th International Conference on Port and Ocean Engineering under Arctic Conditions.

Mäkynen M, Karvonen J, Cheng B, et al. 2020. Operational service for mapping the Baltic Sea landfast ice properties. Remote Sens, 12(24): 4032, doi:10.3390/rs12244032.

Morales Maqueda M A, Willmott A J, Biggs N R T. 2004. Polynya dynamics: a review of observations and modeling. Rev Geophys, 42(1): RG1004, doi:10.1029/2002RG000116.

Marbouti M, Praks J, Antropov O, et al. 2017. A study of landfast ice with Sentinel-1 repeat-pass interferometry over the Baltic Sea. Remote Sens, 9(8): 833, doi:10.3390/rs9080833.

Massom R A, Hill K, Barbraud C, et al. 2009. Fast ice distribution in Adélie Land, East Antarctica: interannual variability and implications for emperor penguins *Aptenodytes forsteri*. Mar Ecol Prog Ser, 374: 243-257, doi:10.3354/meps07734.

Massom R A, Scambos T, Lytle V, et al. 2003. Fast ice distribution and its interannual variability in East Antarctica, determined from satellite data analysis. Dunedin, New Zealand: 16th International Symposium on Ice.

Maykut G A, Untersteiner N. 1971. Some results from a time-dependent thermodynamic model of sea ice. J Geophys Res, 76(6): 1550-1575, doi:10.1029/JC076i006p01550.

Melling H. 2002. Sea ice of the northern Canadian Arctic Archipelago. J Geophys Res Oceans, 107(C11): 2-1, doi:10.1029/2001JC001102.

Meredith M, Sommerkorn M, Cassotta S, et al. 2019. Polar Regions. IPCC Special Report on the Ocean and Cryosphere in a Changing Climate.

Meyer F J, Mahoney A R, Eicken H, et al. 2011. Mapping Arctic landfast ice extent using L-band synthetic aperture radar interferometry. Remote Sens Environ, 115(12): 3029-3043, doi:10.1016/ j.rse.2011.06.006.

Nicolaus M, Haas C, Bareiss J. 2003. Observations of superimposed ice formation at melt-onset on fast ice on Kongsfjorden, Svalbard. Phys Chem Earth Parts A/B/C, 28(28-32): 1241-1248, doi:10.1016/j.pce.2003.08.048.

Olason E. 2016. A dynamical model of Kara Sea land-fast ice. J Geophys Res Oceans, 121(5): 3141-3158, doi:10.1002/2016JC011638.

Peeken I, Primpke S, Beyer B, et al. 2018. Arctic sea ice is an important temporal sink and means of transport for microplastic. Nat Commun, 9: 1505, doi:10.1038/s41467-018-03825-5.

Peng G, Meier W N. 2018. Temporal and regional variability of Arctic sea-ice coverage from satellite data. Ann Glaciol, 59(76pt2): 191-200, doi:10.1017/aog.2017.32.

Petrich C, Eicken H, Zhang J, et al. 2012. Coastal landfast sea ice decay and breakup in northern Alaska: key processes and seasonal prediction.

J Geophys Res Oceans, 117(C2): C02003, doi:10.1029/2011JC007 339.

Polyakov I V, Alekseev G V, Bekryaev R V, et al. 2003. Long-term ice variability in Arctic marginal seas. J Climate, 16(12): 2078-2085, doi:10.1175/1520-0442(2003)016<2078: liviam>2.0.co;2.

Polyakov I V, Walsh J E, Kwok R. 2012. Recent changes of Arctic multiyear sea ice coverage and the likely causes. Bull Amer Meteor Soc, 93(2): 145-151, doi:10.1175/bams-d-11-00070.1.

Qin K, Zhang Y, Gao G P, et al. 2019. Variation of Arctic Ocean runoff and its correlation with coastal sea ice. Chin J Polar Res, (4): 371-382, doi:10.13679/j.jdyj.20180055 (in Chinese with English abstract).

Rachold V, Grigoriev M N, Are F E, et al. 2000. Coastal erosion vs riverine sediment discharge in the Arctic Shelf seas. Int J Earth Sci, 89(3): 450-460, doi:10.1007/s005310000113.

Reimnitz E. 2000. Interactions of river discharge with sea ice in proximity of Arctic deltas: a review. Polarforschung, 70(1): 123-134.

Reimnitz E, Toimil L, Barnes P. 1978. Arctic continental shelf morphology related to sea-ice zonation, Beaufort Sea, Alaska. Mar Geol, 28(3-4): 179-210, doi:10.1016/0025-3227(78)90018-X.

Selyuzhenok V, Krumpen T, Mahoney A, et al. 2015. Seasonal and interannual variability of fast ice extent in the southeastern Laptev Sea between 1999 and 2013. J Geophys Res Oceans, 120(12): 7791-7806, doi:10.1002/2015JC011135.

Selyuzhenok V, Mahoney A, Krumpen T, et al. 2017. Mechanisms of fast-ice development in the south-eastern Laptev Sea: a case study for winter of 2007/08 and 2009/10. Polar Res, 36(1): 1411140, doi:10.1080/17518369.2017.1411140

Shakhova N, Semiletov I, Sergienko V, et al. 2015. The East Siberian Arctic Shelf: towards further assessment of permafrost-related methane fluxes and role of sea ice. Phil Trans R Soc A, 373(2052): 20140451, doi:10.1098/rsta.2014.0451.

Shirasawa K, Leppäranta M, Saloranta T, et al. 2005. The thickness of coastal fast ice in the Sea of Okhotsk. Cold Reg Sci Technol, 42(1): 25-40, doi:10.1016/j.coldregions.2004.11.003.

Solomon S M, Taylor A E, Stevens C W. 2008. Nearshore ground temperatures, seasonal ice bonding, and permafrost formation within the bottom-fast ice zone, Mackenzie Delta, NWT. Fairbanks, Alaska: Proceedings of the Ninth International Conference on Permafrost.

Stauffer B A, Goes J I, McKee K T, et al. 2014. Comparison of spring-time phytoplankton community composition in two cold years from the western Gulf of Alaska into the southeastern Bering Sea. Deep Sea Res Part II Top Stud Oceanogr, 109: 57-70, doi:10.1016/j.dsr2.2014. 03.007.

Stevens C W, Moorman B J, Solomon S M. 2010. Interannual changes in seasonal ground freezing and near-surface heat flow beneath bottom-fast ice in the near-shore zone, Mackenzie Delta, NWT, Canada. Permafr Periglac Process, 21(3): 256-270, doi:10.1002/ ppp.682.

Stringer W J, Barrett S, Schreurs L. 1978. Morphology of Beaufort, Chukchi and Bering seas near shore ice conditions by means of satellite and aerial remote sensing. Environmental assessment of the Alaskan Continental Shelf. Annual Reports of Principal Investigators for the Year Ending March 1978, 10. Vol.X: Transport, Outer Continental Shelf Environmental Assessment Program, 1-220.

Strong C, Rigor I G. 2013. Arctic marginal ice zone trending wider in summer and narrower in winter. Geophys Res Lett, 40(18): 4864-4868, doi:10.1002/grl.50928.

Trishchenko A P, Luo Y. 2021. Landfast ice mapping using MODIS clear-sky composites: application for the Banks Island coastline in Beaufort Sea and comparison with Canadian ice service data. Can J Remote Sens, 47(1): 143-158, doi:10.1080/07038992.2021.1909466.

Wang C, Cheng B, Wang K, et al. 2015. Modelling snow ice and superimposed ice on landfast sea ice in Kongsfjorden, Svalbard. Polar Res, 34(1): 20828, doi:10.3402/polar.v34.20828.

Wang C, Negrel J, Gerland S, et al. 2020. Thermodynamics of fast ice off the northeast coast of Greenland (79°N) over a full year (2012–2013). J Geophys Res Oceans, 125(7): e2019JC015823, doi:10.1029/2019 JC015823.

World Meteorological Organization (WMO). 2014. WMO sea ice nomenclature (WMO No. 259, volume 1 – Terminology and Codes) . https://library.wmo.int/doc_num.php?explnum_id=4651.

Yang Y, Leppäranta M, Li Z J, et al. 2015. Model simulations of the annual cycle of the landfast ice thickness in the East Siberian Sea. Adv Polar Sci, 26(2): 168-178, doi: 10.13679/j.advps.2015.2.00168.

Yu Y, Stern H, Fowler C, et al. 2014. Interannual variability of Arctic landfast ice between 1976 and 2007. J Clim, 27(1): 227-243, doi:10.1175/jcli-d-13-00178.1.

Zhai M, Cheng B, Leppäranta M, et al. 2021. The seasonal cycle and break-up of landfast sea ice along the northwest coast of Kotelny Island, East Siberian Sea. J Glaciol, 1-13, doi:10.1017/jog.2021.85.

Zhao J, Cheng B, Vihma T, et al. 2019. Observation and thermodynamic modeling of the influence of snow cover on landfast sea ice thickness in Prydz Bay, East Antarctica. Cold Reg Sci Technol, 168: 102869, doi:10.1016/j.coldregions.2019.102869.

Zhao J, Cheng B, Vihma T, et al. 2020. Fast Ice Prediction System (FIPS) for land-fast sea ice at Prydz Bay, East Antarctica: an operational service for CHINARE. Ann Glaciol, 61(83): 271-283, doi:10.1017/ aog.2020.46.